

9. Fraser, P. *et al.* Lifetime and emission estimates of 1,1,2-trichlorotrifluoroethane (CFC-113) from daily global background observations June 1982–June 1994. *J. Geophys. Res.* **101**, 12585–12599 (1996).
10. Simmonds, P. G. *et al.* Global trends and emission estimates of CCl₄ from in situ background observations from July 1978 to June 1996. *J. Geophys. Res.* **103**, 16017–16028 (1998).
11. Prinn, R. G. *et al.* Atmospheric trends and lifetime of CH₂Cl₂ and global OH concentrations. *Science* **269**, 187–192 (1995).
12. Butler, J. H. *et al.* Growth and distribution of halons in the atmosphere. *J. Geophys. Res.* **103**, 1503–1511 (1998).
13. Prather, M. J. & Watson, R. T. Stratospheric ozone depletion and future levels of atmospheric chlorine and bromine. *Nature* **344**, 729–734 (1990).
14. Daniel, J. S., Solomon, S. & Albritton, D. L. On the evaluation of halocarbon radiative forcing and global warming potentials. *J. Geophys. Res.* **100**, 1271–1285 (1995).
15. Jackman, C. H. *et al.* Past, present, and future modeled ozone trends with comparisons to observed trends. *J. Geophys. Res.* **101**, 28753–28767 (1996).
16. Portmann, R. W. *et al.* Role of aerosol variations in anthropogenic ozone depletion in the polar regions. *J. Geophys. Res.* **101**, 22991–23006 (1996).
17. Solomon, S. *et al.* The role of aerosol variations in anthropogenic ozone depletion at northern midlatitudes. *J. Geophys. Res.* **101**, 6713–6727 (1996).
18. Shindell, D. T., Rind, D. & Loneragan, P. Increased polar stratospheric ozone loss and delayed eventual recovery owing to increasing greenhouse-gas concentrations. *Nature* **392**, 589–592 (1998).
19. McCulloch, A. Global production and emissions of bromochlorodifluoromethane and bromotrifluoromethane (halons 1211 and 1301). *Atmos. Environ.* **A 26**, 1325–1329 (1992).
20. UNEP Technology and Economic Assessment Panel April 1998 Report (United Nations Environment Programme, Nairobi, Kenya, 1998); also available at (http://www.teap.org/html/teap_reports.html).
21. Prather, M. J. *et al.* in *Climate Change 1995, the Science of Climate Change* (eds Houghton, J. T. *et al.*) Ch. 33 (Cambridge Univ. Press, 1996).
22. Report of the Halon Fire Extinguishing Agents Technical Options Committee (United Nations Environment Programme, Nairobi, Kenya, 1994).
23. Volk, C. M. *et al.* Evaluation of source gas lifetimes from stratospheric observations. *J. Geophys. Res.* **102**, 25543–25564 (1997).
24. Burkholder, J. B. *et al.* Atmospheric fate of CF₃Br, CF₂Br₂, CF₂ClBr, and CF₂BrCF₂Br. *J. Geophys. Res.* **96**, 5025–5043 (1991).
25. Butler, J. H. *et al.* A decrease in the growth rates of atmospheric halon concentrations. *Nature* **359**, 403–405 (1992).
26. Montzka, S. A. *et al.* Global tropospheric distribution and calibration scale of HCFC-22. *Geophys. Res. Lett.* **20**, 703–706 (1993).
27. Montzka, S. A. *et al.* Early trends in the global tropospheric abundance of hydrochlorofluorocarbon-141b and -142b. *Geophys. Res. Lett.* **21**, 2483–2486 (1994).
28. Trenberth, K. E. & Guillemot, C. J. The total mass of the atmosphere. *J. Geophys. Res.* **99**, 23079–23088 (1994).
29. Fraser, P. J. *et al.* Southern hemispheric halon trends (1978–1998) and global halon emissions. *J. Geophys. Res.* (in the press).

Acknowledgements. We thank all personnel involved in collecting flask samples at the NOAA/CMDL Observatories and at cooperative sampling sites. S.A.M. appreciates discussions and suggestions from S. Solomon and P. Midgley, and we appreciate the past technical assistance of R. C. Myers and T. H. Swanson. This work was supported in part by NOAA's Radiatively Important Trace Species research and by the Atmospheric Chemistry project of the NOAA Climate and Global Change Program.

Correspondence and requests for materials should be addressed to S.A.M. (e-mail: smontzka@cmdl.noaa.gov). Data used in this Letter are available at (<http://www.cmdl.noaa.gov/ftpdata.html>) or (<ftp://ftp.cmdl.noaa.gov/noah>).

Increased El Niño frequency in a climate model forced by future greenhouse warming

A. Timmermann, J. Oberhuber*, A. Bacher, M. Esch, M. Latif & E. Roeckner

Max-Planck-Institut für Meteorologie und * Deutsches Klimarechenzentrum, Bundesstrasse 55, D-20146 Hamburg, Germany

The El Niño/Southern Oscillation (ENSO) phenomenon is the strongest natural interannual climate fluctuation¹. ENSO originates in the tropical Pacific Ocean and has large effects on the ecology of the region, but it also influences the entire global climate system and affects the societies and economies of many countries². ENSO can be understood as an irregular low-frequency oscillation between a warm (El Niño) and a cold (La Niña) state. The strong El Niños of 1982/1983 and 1997/1998, along with the more frequent occurrences of El Niños during the past few decades, raise the question of whether human-induced 'greenhouse' warming affects, or will affect, ENSO³. Several global climate models have been applied to transient greenhouse-gas-induced warming simulations to address this question^{4–6}, but the results have been debated owing to the inability of the models to fully simulate ENSO (because of their coarse equatorial resolution)⁷. Here we present results from a global climate

model with sufficient resolution in the tropics to adequately represent the narrow equatorial upwelling and low-frequency waves. When the model is forced by a realistic future scenario of increasing greenhouse-gas concentrations, more frequent El Niño-like conditions and stronger cold events in the tropical Pacific Ocean result.

Our global climate model^{8,9} uses a meridional resolution of 0.5° in the tropics. The model, which is 'flux corrected', simulates an irregular ENSO cycle similar to the observed one, and the amplitude and dynamics of the simulated ENSO cycle are consistent with those derived from observations^{8,9}. The simulated ENSO period is too short, however, and amounts to about two years, whereas observations indicate a main period of about four years. Our model successfully predicted the onset and decline of the 1997/1998 El Niño several months in advance¹⁰.

Here, two experiments were performed. The first experiment is a 300-year-long control integration with fixed present-day atmospheric concentrations of greenhouse gases. The second experiment is a transient greenhouse warming simulation in which the model was forced by increasing levels of greenhouse gases as observed (1860–1990) and according to IPCC scenario IS92a¹¹ (1990–2100).

The changes in the mean state at the surface of the tropical Pacific Ocean, as derived from the transient greenhouse warming simulation, are reminiscent of the anomalous climate state observed during present-day El Niño conditions (Fig. 1). The sea-surface-temperature (SST) trend pattern is characterized by strongest warming in the equatorial east Pacific, accompanied by westerly near-surface wind anomalies in the equatorial region to the west of the maximum warming and strong equatorward flow off the Equator (not shown). The associated trend in rainfall is rather similar to that simulated during present-day El Niños (not shown).

There has been some discussion about the relative roles of different feedbacks involved in the time-mean response of the tropical Pacific climate system to greenhouse warming. On the one hand, it has been suggested that regional differences in the cloud-albedo feedback will lead to surface warming that is strongest in the equatorial east Pacific¹². The argument is that the equatorial west Pacific is so warm that even modest additional warming would lead to a cloud shielding effect, with high cirrus clouds, reducing incoming solar radiation at the surface and inhibiting further warming¹³. This 'thermostat' would be less efficient in the eastern equatorial Pacific, so it would warm more than the western Pacific. This would lead to a slackening of the winds along the Equator and

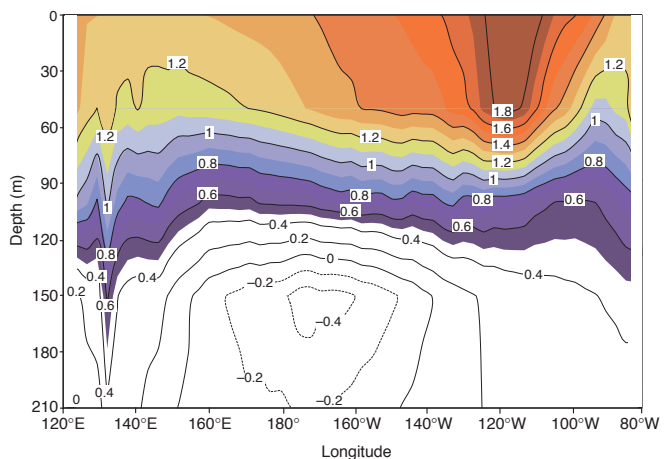


Figure 1 Simulated temperature trends in equatorial waters. The linear trends in the temperatures of the upper 210 m of the Pacific Ocean at the Equator (°C rise per 100 years) are derived from the full (240-year-long) transient greenhouse warming simulation. There is a warming trend near the surface and a cooling trend at deeper levels, leading to a stronger thermocline. The trends at the surface resemble the anomalous conditions observed during present-day El Niños.

result in overall conditions very similar to those observed during El Niños.

On the other hand, it has been argued that the strong equatorial upwelling in the eastern equatorial Pacific will weaken the warming in this region, so the strongest warming will occur in the western equatorial Pacific⁷. This would lead to stronger winds along the Equator, more equatorial upwelling and a net cooling in the eastern Pacific. This 'dynamical thermostat' will lead to overall conditions resembling those observed during La Niñas, eventually retarding global warming. The global climate models applied so far to greenhouse warming simulations could not adequately address this problem⁷ as they were poor at resolving the equatorial upwelling. Our climate model includes adequate representations of both types of feedback, and the balance of all physical processes leads to a simulated warming pattern that is strongest in the east, consistent with ref. 12.

As can be seen from the time evolution of the eastern equatorial SST in the transient greenhouse warming simulation, there is considerable interannual variability superimposed on the warming trend in the tropical Pacific (Fig. 2). Our model simulates an irregular ENSO cycle under enhanced greenhouse conditions, with a main period close to that derived from the control integration. However, the ENSO cycle evolves under different mean conditions to those currently found so we may expect the statistics of the ENSO cycle to change under enhanced greenhouse conditions. It can be seen from the SST time series (Fig. 2) that the level of the interannual variability increases strongly towards the end of the greenhouse warming simulation. This is also seen in the time series of the interannual SST standard deviations, which shows a strong increase towards the end of the transient greenhouse warming integration (Fig. 3). The observations also show that the interannual variability has intensified during the past several decades (Fig. 3), but this is well within the range of our control simulation.

The statistical significance of the increase in ENSO variability is an important issue to be addressed. In addition to our 300-year

control integration, we can use the first 100 years of the scenario integration in the estimation of the natural variability as the external forcing is small up to 1960. We also performed two scenario integrations that included anthropogenic sulphate aerosols¹⁴, which started in 1860 and were integrated up to the year 2050 (not shown). Although these two runs are too short to study changes in the statistics of the interannual variability, their first 100 years can be used in the estimation of the noise, so we have 600 years in total. We did not find any period within the whole 600 years that exceeds a running standard deviation of 1.15 °C. The enhanced ENSO variability seen towards the end of our greenhouse warming integration (Fig. 3) is therefore highly significant.

To investigate further the changes in the ENSO statistics, we computed the frequency distributions of monthly SST anomalies. The distribution obtained from the first half of the transient integration is narrower than that obtained from the second half, so the year-to-year variability becomes more extreme under enhanced greenhouse conditions. Furthermore, although the distributions of the SST anomalies in the control integration (not shown) and during the first half of the transient integration are almost symmetric (Fig. 2c), the distribution for the second half of the transient integration is skewed: strong cold extremes become more frequent, while the statistics of the strong warm extremes do not change (Fig. 2d).

Which changes in the mean state lead to changes in the statistics of the interannual variability? First, the changes in the mean state near the surface (Fig. 1) could favour a reduction in ENSO-type variability as the zonal asymmetries across the equatorial Pacific are reduced¹⁵. Second, interactions between the air and the sea may be more energetic in a warmer climate, increasing the interannual variability. Third, changes in the vertical density structure of the ocean may alter the level of the interannual variability. The equatorial thermocline becomes stronger in response to greenhouse warming (Fig. 1): temperatures near the surface rise, but those at deeper ocean levels fall. This cooling at subsurface levels can be

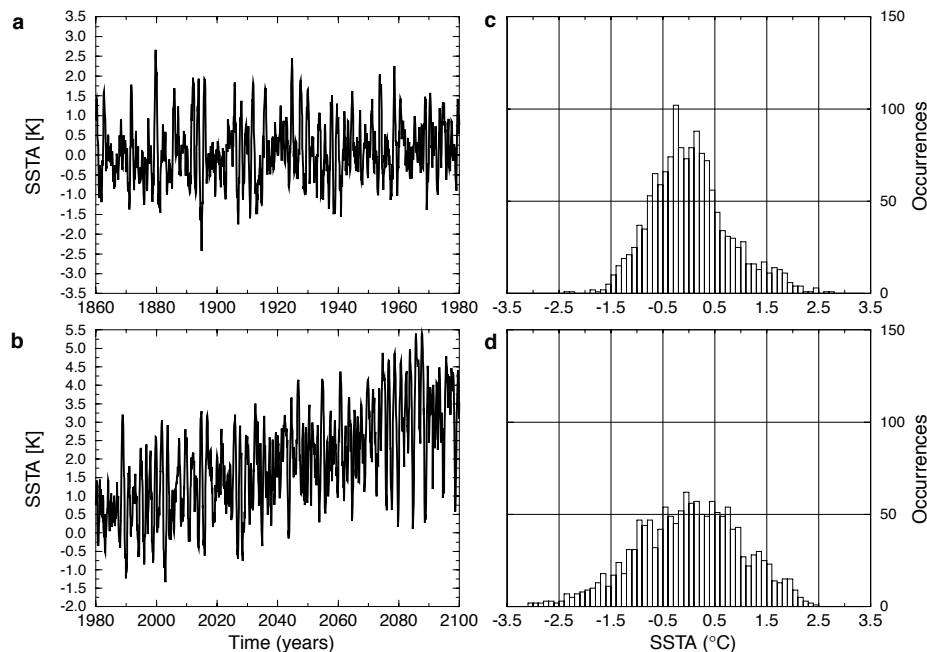


Figure 2 Simulated sea-surface-temperature anomalies. **a, b**, Time series of eastern equatorial SST anomalies (SSTA; relative to the control run) averaged over the Niño-3 region (150°W–90°W, 5°N–5°S) (°C) during the first half (**a**) and second half (**b**) of the transient greenhouse warming simulation. **c, d**, Frequency distribution of Niño-3 SST anomalies during the first half (**c**) and second half (**d**) of the transient greenhouse warming simulation. Anomalies were computed by subtracting the linear trends and means from the time series of eastern equatorial

Pacific SSTs and by removing the mean annual cycle of the control integration. Note the change in the frequency distributions from the first to the second half of the transient integration. The distribution is almost symmetric (with a small bias towards the warm side) during the first half (and during the control integration; not shown), but is biased towards the cold side during the second half of the transient integration: strong cold events become more frequent.

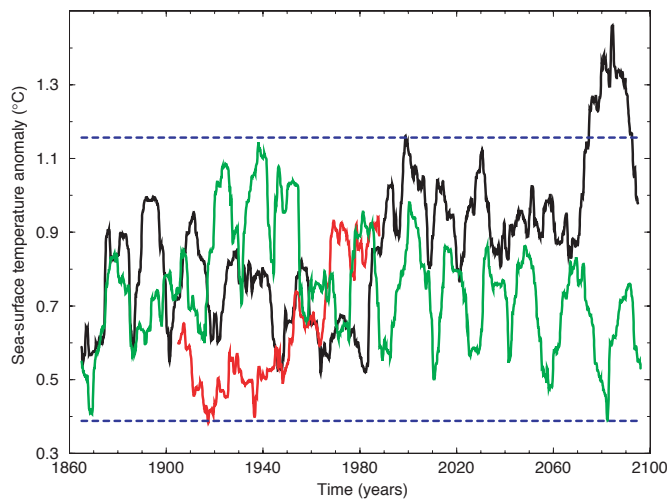


Figure 3 Interannual variability of observed and simulated SST anomalies. Standard deviations of Niño-3 SST anomalies (°C) as function of time during the transient greenhouse warming simulation (black). Also shown are the time evolutions of the standard deviation of the observed (red) and control run (green) Niño-3 SST anomalies. A low-pass filter in the form of a sliding window 10 years wide was used to compute the standard deviations. Both the simulated and observed SST anomalies exhibit trends towards stronger interannual variability, with pronounced interdecadal variability superimposed. The minimum and maximum standard deviations derived from the control run with present-day concentrations of greenhouse gases are denoted by the dashed lines.

attributed to a greater inflow of cold waters in response to the intensification of the atmospheric Hadley Circulation, especially in the Southern Hemisphere. In order to gain further insight into the dynamics of the changes in the ENSO statistics, we computed atmospheric and oceanic sensitivities as functions of time (Fig. 4). The most important atmospheric forcing for equatorial oceans is the zonal wind stress component. We computed first the sensitivity of central equatorial zonal wind stress anomalies to the SST anomalies in the eastern equatorial Pacific averaged over the Niño-3 region (150°W–90°W, 5°N–5°S). No significant change was found. We then computed the sensitivity of Niño-3 SST anomalies to changes in the central equatorial zonal wind stress. This exhibited a significant increase towards the end of the transient greenhouse warming simulation, indicating that changes in the ocean dynamics arising from the strengthening thermocline are responsible for the enhanced interannual variability. This result is consistent with findings obtained from simpler coupled models^{16–18}.

The simple models also predict a skew in the frequency distribution of the thermocline depth anomalies in the eastern equatorial Pacific (a quantity closely related to eastern equatorial SST anomalies) for a sharpening thermocline, with strong cold events becoming more frequent¹⁸. This is consistent with our greenhouse warming simulation (Fig. 2). We therefore conclude that the most important change in the mean state of the tropical Pacific Ocean–atmosphere system affecting the ENSO statistics appears to be the strengthening of the equatorial thermocline.

The tropical Pacific climate system is thus predicted to undergo strong changes if emissions of greenhouse gases continue to increase. The climatic effects will be threefold. First, the mean climate in the tropical Pacific region will change towards a state corresponding to present-day El Niño conditions. It is therefore likely that events typical of El Niño will also become more frequent. Second, a stronger interannual variability will be superimposed on the changes in the mean state, so year-to-year variations may become more extreme under enhanced greenhouse conditions. Third, the interannual variability will be more strongly skewed, with strong cold events (relative to the warmer mean state)

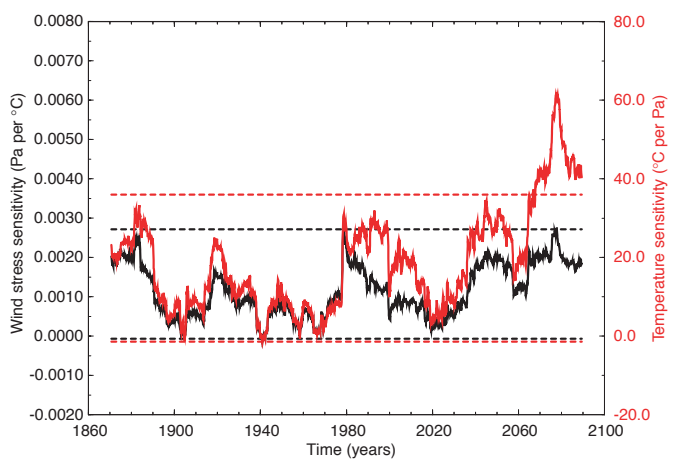


Figure 4 Atmospheric and oceanic model sensitivity. Sensitivity of central equatorial zonal wind stress anomalies (averaged over the region 100°W–160°W, 1.4°N–1.4°S) to changes in the Niño-3 SST anomalies as function of time during the transient greenhouse warming simulation (black). The atmospheric sensitivity is defined as the covariance of the zonal wind stress and Niño-3 SST anomalies divided by the variance of the Niño-3 SST anomalies (Pa per °C). Also shown is the sensitivity of eastern equatorial SST anomalies averaged over the Niño-3 region to the central equatorial zonal wind stress anomalies averaged over the region indicated above (red). The oceanic sensitivity is defined as the covariance of the zonal wind stress and Niño-3 SST anomalies divided by the variance of the zonal wind stress anomalies (°C per Pa). A sliding window 10 years wide was used to compute the sensitivities. The minima and maxima derived from the control run are shown by the dashed black and red lines, respectively. Only the temperature sensitivity exhibits a statistically significant increase, indicating that the changes in the ocean dynamics in response to the strengthening thermocline are responsible for the increase in the level of the interannual variability.

becoming more frequent. Although the model was successful in simulating and predicting ENSO, the ENSO response to greenhouse warming may depend on processes that are not well understood, such as cloud feedback, so we cannot exclude the possibility that the results are sensitive to the model formulation. □

Received 21 December 1998; accepted 22 February 1999.

- Philander, S. G. H. *El Niño, La Niña, and the Southern Oscillation* (Academic, San Diego, 1990).
- Glantz, M. H., Katz, R. W. & Nicholls, N. *Teleconnections Linking Worldwide Climate Anomalies* (Cambridge Univ. Press, 1991).
- Trenberth, K. & Hoar, T. The 1990–1995 El Niño–Southern Oscillation event: Longest on record. *Geophys. Res. Lett.* **23**, 57–60 (1996).
- Knutson, T. R., Manabe, S. & Gu, D. Simulated ENSO in a global coupled ocean–atmosphere model: multidecadal amplitude modulation and CO₂ sensitivity. *J. Clim.* **10**, 138–161 (1997).
- Tett, S. Simulation of El Niño–Southern Oscillation-like variability in a global AOGCM and its response to CO₂ increase. *J. Clim.* **8**, 1473–1502 (1995).
- Meehl, G. A., Branstator, G. W. & Washington, W. M. Tropical Pacific interannual variability and CO₂ climate change. *J. Clim.* **6**, 42–63 (1993).
- Cane, M. A. *et al.* Twentieth-century sea surface temperature trends. *Science* **275**, 957–960 (1997).
- Roeckner, E., Oberhuber, J. M., Bacher, A., Christoph, M. & Kirchner, I. ENSO variability and atmospheric response in a global atmosphere–ocean GCM. *Clim. Dynam.* **12**, 737–754 (1996).
- Bacher, A., Oberhuber, J. M. & Roeckner, E. ENSO dynamics and seasonal cycle in the tropical Pacific as simulated by the ECHAM4/OPYC3 coupled general circulation model. *Clim. Dynam.* **14**, 431–450 (1997).
- Oberhuber, J. M., Roeckner, E., Christoph, M., Esch, M. & Latif, M. Predicting the '97 El Niño event with a global climate model. *Geophys. Res. Lett.* **25**, 2273–2276 (1998).
- Houghton, J. T., Callander, B. A. & Varney, S. K. V. (eds) *IPCC Climate Change 1992. The Supplementary Report to the IPCC Scientific Assessment* (Cambridge Univ. Press, 1992).
- Meehl, G. A. & Washington, W. M. El Niño-like climate change in a model with increased atmospheric CO₂ concentrations. *Nature* **382**, 56–60 (1996).
- Ramanathan, V. & Collins, W. Thermodynamic regulation of ocean warming by cirrus clouds deduced from observations of the 1987 El Niño. *Nature* **351**, 27–32 (1991).
- Roeckner, E., Bengtsson, L., Feichter, J., Lelieveld, J. & Rodhe, H. Transient climate change simulations with a coupled atmosphere–ocean GCM including the sulfur cycle. *J. Clim.* (in the press).
- Battisti, D. S. & Hirst, A. C. Interannual variability in the tropical atmosphere/ocean system: Influence of the basic state, ocean geometry and non-linearity. *J. Atmos. Sci.* **46**, 1687–1712 (1989).
- Münnich, M., Cane, M. A. & Zebia, S. E. A study of self-excited oscillations of the tropical ocean–atmosphere system, Part II: Nonlinear cases. *J. Atmos. Sci.* **48**, 1238–1248 (1991).
- Tziperman, E., Stone, L., Cane, M. A. & Jarosh, H. El Niño chaos: overlapping of resonances between the seasonal cycle and the Pacific Ocean–Atmosphere Oscillator. *Science* **264**, 72–74 (1994).
- Stone, L., Saparin, P. I., Huppert, A. & Price, C. El Niño chaos: The potential role of noise and stochastic resonance on the ENSO cycle. *Geophys. Res. Lett.* **25**, 175–178 (1998).

Acknowledgements. We thank T. P. Barnett for discussion and M. Münnich for help with data processing. This work was sponsored by the German government under its programme 'Klimavariabilität und Signalanalyse' and by the European Union through its 'SINTEX' programme. The climate model integrations were performed at the Deutsches Klimarechenzentrum.

Correspondence and requests for materials should be addressed to M.L. (e-mail: latif@dkrz.de).

Continental-shelf sediment as a primary source of iron for coastal phytoplankton

Kenneth S. Johnson*†, Francisco P. Chavez† & Gernot E. Friederich†

* Moss Landing Marine Laboratories, PO Box 450, Moss Landing, California 95039, USA

† Monterey Bay Aquarium Research Institute, PO Box 628, Moss Landing, California 95039, USA

The availability of iron, an essential nutrient, controls rates of phytoplankton primary productivity in the open-ocean, upwelling ecosystems of the equatorial Pacific^{1,2}. Upwelling injects large amounts of macronutrients into the euphotic zone of eastern boundary currents, such as the California Current System (CCS), where iron can become the limiting factor on productivity^{3,4}. Iron addition to samples from some areas of the CCS has been shown to increase rates of biomass production^{5,6}, but the processes that control iron availability in these systems remain poorly understood. Here we report measurements of dissolvable iron (that is, dissolved plus leachable iron at pH 3) in transects across the CCS in March of 1997 and 1998. We found high concentrations of iron in 1997 during strong upwelling conditions. During the 1998 El Niño, the concentration of dissolvable iron in surface waters was low, even though that year was marked by high river flow and low offshore salinity. These results indicate that the primary source of iron in the CCS is resuspension of particles in the benthic boundary layer, followed by upwelling of this iron-rich water, rather than direct riverine input. This source of iron must be an essential but variable component of the high productivity found in upwelling ecosystems.

Upwelling along eastern boundary currents sustains some 11% of the global ocean primary production⁷ and 50% of the global fish production⁸. The waters that come to the surface in these systems are enriched in macronutrients. However, there is no corresponding subsurface enrichment of iron in the offshore areas that are the source of the upwelled waters³. Consequently, there must be additional sources of iron at the continental margin to sustain elevated rates of primary production. Large concentration gradients of dissolved and particulate iron across both eastern⁹ and western¹⁰ ocean boundaries demonstrate that ocean margins are important sources of iron. It has been hypothesized that elevated iron concentrations in coastal regions may arise from riverine input, resuspended sediment or atmospheric deposition⁹, but so far we do not know the relative importance of these mechanisms or how they vary over time.

We have made measurements of dissolvable iron, nitrate and chlorophyll in March 1997 (cruise S197) and March 1998 (cruise S298) at a depth of 2 m along transects from Monterey Bay in a southwesterly direction across the CCS (Fig. 1). Conditions in March of 1997 were representative of typical spring upwelling, with strong winds from the northwest (Fig. 2c). A sharp drop in surface temperature, driven by strong winds that favoured upwelling, was recorded just before the S197 cruise at the MBARI M1 mooring in Monterey Bay¹¹ (Fig. 2a). Temperatures remained low throughout the cruise and dissolved nitrate concentrations near the

surface were as high as 25 μM . Surface salinities measured along the transect were >32.8 , which is typical of the CCS in this region¹². The shipboard measurements of dissolvable iron at stations within 100 km of the coast averaged 6 nM, but values as high as 20 nM were observed near the core of the upwelling system at Año Nuevo, which feeds Monterey Bay¹³. In the open ocean waters more than 200 km offshore (west of 124.2° W), the dissolvable iron concentration was 0.2 ± 0.1 (mean \pm standard deviation) nM. High chlorophyll concentrations developed near the coast under these conditions (Fig. 1c).

Wind conditions that favoured upwelling were rare during the El Niño conditions of late winter and early spring of 1998. High-wind events were primarily from the south (Fig. 2c), which would have suppressed offshore transport, and the surface ocean was nearly 3 °C

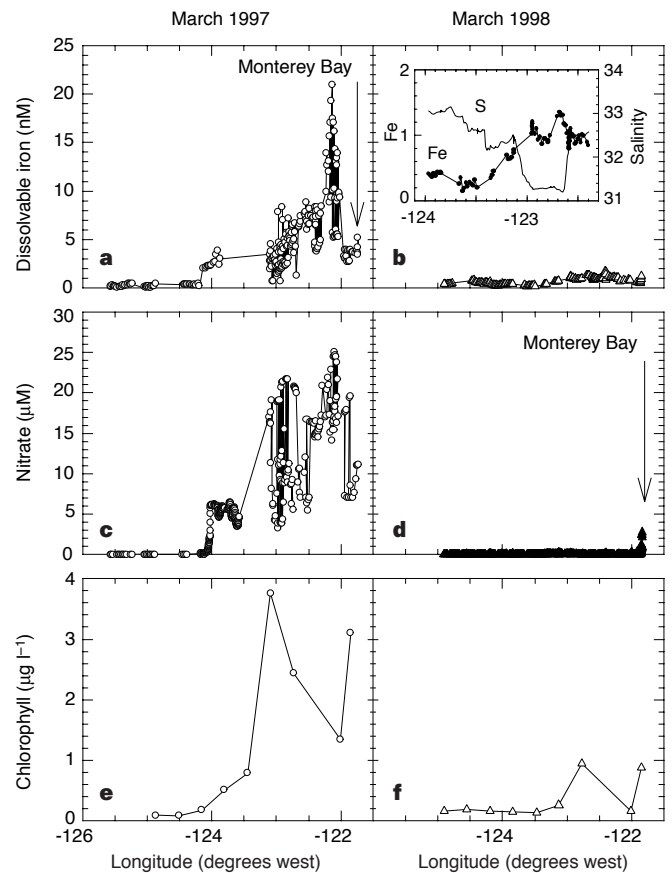


Figure 1 Dissolvable iron, nitrate and chlorophyll on transects across the CCS. Measurements were made from Moss Landing in Monterey Bay (36.80° N, 121.79° W) to a point 390 km offshore (35.07° N, 125.57° W) on cruise S197 (3–9 March 1997) and 317 km offshore (35.46° N, 124.90° W) on cruise S298 (March 18–23 1998). The inset to **b** shows iron concentration on an expanded scale and the salinity on S298, which is anomalously low over the inner 150 km. Dissolvable iron was measured by flow-injection analysis with chemiluminescence detection at 6-min intervals²⁴. Sea water was sampled with an all-TEFLON pump system towed at 1–2 m depth. Nitrate in this sample stream was determined colorimetrically aboard ship using an automated continuous-flow analysis system²⁵. Sea water from the pump was passed through a 10- μm polypropylene filter and acidified to pH 3 for ~ 0.5 min before iron analysis. Laboratory experiments demonstrate no difference between the amount of iron desorbed from particles at pH 3 in 1 min and in >6 h²⁶, indicating that we detected dissolved plus all adsorbed iron. The dissolvable iron/nitrate relationship in the data was similar to that reported previously for Monterey Bay⁹. Chlorophyll was determined by extracting the pigment and measuring fluorescence in a shore-based laboratory. The nitrate data near the upwelling front at 124° W on S197 were obtained on the inshore leg of the cruise to replace data missing on the offshore transect.